


## Superconductivity by alloying the topological insulator $\text{SnBi}_2\text{Te}_4$

Michael A. McGuire<sup>1,\*</sup>, Heda Zhang<sup>1</sup>, Andrew F. May<sup>1</sup>, Satoshi Okamoto<sup>1</sup>, Robert G. Moore<sup>1</sup>, Xiaoping Wang<sup>2</sup>, Clément Girod<sup>3</sup>, Sean M. Thomas<sup>3</sup>, Filip Ronning<sup>3</sup>, and Jiaqiang Yan<sup>1</sup>

<sup>1</sup>Materials Science and Technology Division, Oak Ridge National Laboratory, Oak Ridge, Tennessee 37831, USA

<sup>2</sup>Neutron Scattering Division, Oak Ridge National Laboratory, Oak Ridge, Tennessee 37831, USA

<sup>3</sup>Los Alamos National Laboratory, Los Alamos, New Mexico 87545, USA

 (Received 22 September 2022; revised 24 February 2023; accepted 22 March 2023; published 31 March 2023)

Alloying indium into the topological insulator  $\text{SnBi}_2\text{Te}_4$  induces bulk superconductivity with critical temperatures  $T_c$  up to 1.85 K and upper critical fields up to about 14 kOe. This is confirmed by electrical resistivity, heat capacity, and magnetic susceptibility measurements. The heat capacity shows a discontinuity at  $T_c$  and temperature dependence below  $T_c$  consistent with weak coupling BCS theory, and suggests a superconducting gap near 0.25 meV. The superconductivity is type-II and the topological surface states have been verified by photoemission. A simple picture suggests analogies with the isostructural magnetic topological insulator  $\text{MnBi}_2\text{Te}_4$ , in which a natural heterostructure hosts complementary properties on different sublattices, and motivates new interest in this large family of compounds. The existence of both topological surface states and superconductivity in  $\text{Sn}_{1-x}\text{In}_x\text{Bi}_2\text{Te}_4$  identifies these materials as promising candidates for the study of topological superconductivity.

DOI: [10.1103/PhysRevMaterials.7.034802](https://doi.org/10.1103/PhysRevMaterials.7.034802)

### I. INTRODUCTION

Designing new quantum materials, and functional materials in general, often requires combining multiple phenomena or behaviors into a single sample or system. This is true for topological materials, where combining topology with magnetism can generate Weyl semimetals and Chern and axion insulators [1–4], and combining topology with superconductivity can produce Majorana zero modes [5–8]. These combinations can be achieved in several ways, and are often realized in designer heterostructures where dissimilar materials are physically stacked or grown together as thin films or nanostructures [3,8,9]. In some cases, functionalities can be combined in a single material [1,10]. One approach is to employ crystal structures that have separate sublattices that each host one of the desired behaviors. An excellent example of this is given by the combination of magnetism and topology in  $\text{MnBi}_2\text{Te}_4$  and related materials [11,12]. The crystal structures of these compounds contain ordered arrangements of magnetic MnTe layers and topological  $\text{Bi}_2\text{Te}_3$  layers. This has led to intense study of these materials and reports of Chern and axion insulating behavior, and the quantum anomalous Hall effect [13–17].

Combining topology with superconductivity is expected to be possible in triplet or  $p$ -wave superconductors [6,18], but the more common approach is based on the Fu-Kane model, in which the spin-momentum locked surface states in a topological insulator interact with the  $s$ -wave superconductivity in another material via proximity effects [5]. These two phenomena may arise from separate sources in a single

material, giving rise to an intrinsic proximity effect, for example when a topological semimetal becomes superconducting. The iron-based superconductor  $\text{FeSe}_{1-x}\text{Te}_x$  is an example of this, with topological surface states related to the strong spin orbit coupling of Te and superconductivity related primarily to Fe [10,19].

Here we explore this idea using the same materials family to which  $\text{MnBi}_2\text{Te}_4$  belongs. This family, typified by the  $\text{GeAs}_2\text{Te}_4$  structure type, contains  $AM_2X_4$  with  $A = \text{Mn, Ge, Sn, Pb}$ ,  $M = \text{As, Sb, Bi}$ , and  $X = \text{Se, Te}$ . The structure of  $\text{SnBi}_2\text{Te}_4$  is shown in Fig. 1(a). Since these compounds are formally charge balanced and contain many heavy main group elements, they form small band gap semiconductors with strong spin-orbit coupling. Thus, they have attracted attention for their thermoelectric performance [20–22] and more recently for their electronic topology. Electronic structure calculations show that this family contains many topologically nontrivial compounds [23–27]. Topological surface states have been observed experimentally in  $\text{GeSb}_2\text{Te}_4$  [28],  $\text{GeBi}_2\text{Te}_4$  [29–31],  $\text{SnBi}_2\text{Te}_4$  [31,32],  $\text{SnSb}_2\text{Te}_4$  [33], and  $\text{PbBi}_2\text{Te}_4$  [34]. The present paper concerns specifically  $\text{SnBi}_2\text{Te}_4$  [35,36], which has been identified as a 3D topological insulator based on parity of the valence band states at the  $\Gamma$  point and the observation of topological surface states with angle resolved photoemission spectroscopy (ARPES) measurements [24–26,31,32]. The electronic structure calculations and ARPES data suggest  $\text{SnBi}_2\text{Te}_4$  is a small band gap semiconductor or semimetal, with Dirac surface states overlapping the bulk valence band.

A simple idea for introducing superconductivity into this family is to identify a superconductor among (Ge,Sn,Pb)(Se,Te) compounds and use this to form the layer between the  $\text{Bi}_2\text{Te}_3$  slabs in  $\text{ABi}_2\text{Te}_4$ . Note that

\*mcguirema@ornl.gov

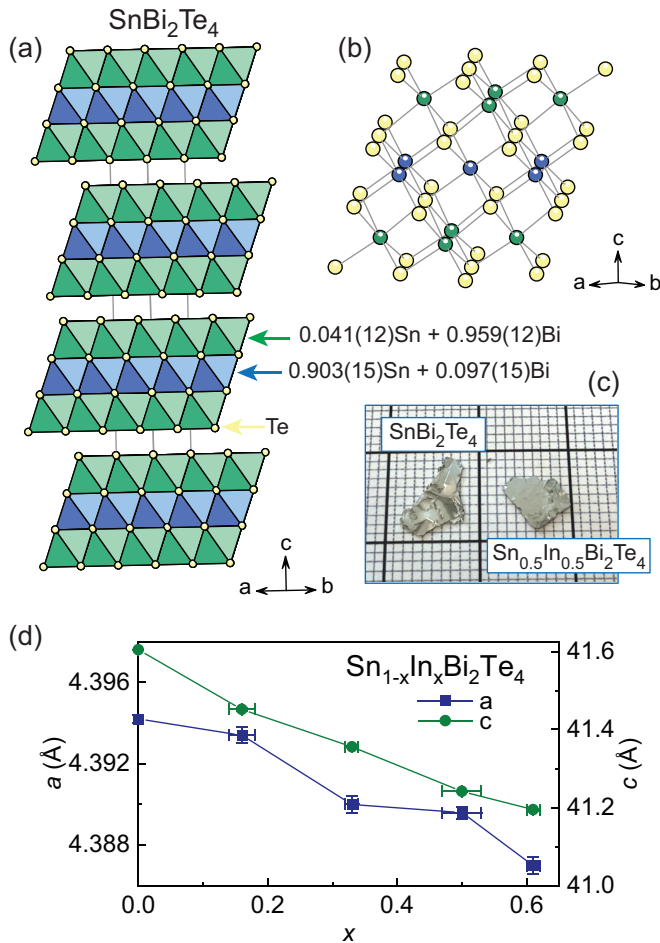


FIG. 1. Structure of  $\text{Sn}_{1-x}\text{In}_x\text{Bi}_2\text{Te}_4$ . (a) A view of the stacking of the septuple layers with cation site occupancies for  $\text{SnBi}_2\text{Te}_4$  ( $x = 0$ ) determined by neutron single crystal diffraction. (b) The internal structure of the septuple layers showing the octahedral coordination environments. (c) Crystals with  $x = 0$  and  $0.5$  on a mm/cm grid. (d) The  $x$  dependence of the lattice parameters determined by powder x-ray diffraction at room temperature.

these binary compounds adopt the rocksalt structure or variants of the rocksalt structure, and the  $\text{AX}_2$  layer at the center of the septuple layer in  $\text{AM}_2\text{X}_4$  can be viewed as a slab excised from the rocksalt structure normal to the [111] direction. Fortunately, there are reports of tuning some of these binary compounds into superconducting states by alloying. This includes  $\text{Pb}_{1-x}\text{Tl}_x\text{Te}$  ( $T_c \approx 1.5$  K) [37],  $\text{Pb}_{1-x}\text{In}_x\text{Te}$  ( $T_c \approx 4.8$  K) [38,39], and  $\text{Sn}_{1-x}\text{In}_x\text{Te}$  ( $T_c \approx 4.7$  K) [40,41]. Here we employ indium-tin alloying to tune the electronic ground state in the topological insulator  $\text{SnBi}_2\text{Te}_4$ .

In this paper, we show that indium substitution does induce superconductivity in  $\text{Sn}_{1-x}\text{In}_x\text{Bi}_2\text{Te}_4$ . The superconductivity is bulk and robust in the single crystals grown for this study. This is evidenced by sharp transitions to zero resistance, large volume fractions inferred from strong diamagnetism, and sharp and large specific heat capacity anomalies. The heat capacity shows behavior consistent with weak coupling BCS theory and a single superconducting gap. For the highest

indium content achieved here ( $x = 0.61$ ),  $T_c$  reaches 1.85 K, with a maximum upper critical field near 14 kOe. The dependence of  $T_c$  on  $x$  suggests higher transition temperatures could be realized at higher indium concentrations. The expected topological surface states are confirmed by ARPES measurements for  $x = 0.5$ , in analogy with the parent phase  $\text{SnBi}_2\text{Te}_4$ . Thus, this work establishes  $\text{Sn}_{1-x}\text{In}_x\text{Bi}_2\text{Te}_4$  as an interesting candidate topological superconductor, and motivates detailed spectroscopic studies to investigate the coupling between superconductivity and topology and the potential presence of Majorana zero modes.

## II. METHODS

Single crystals of  $\text{SnBi}_2\text{Te}_4$  were grown out of Te flux. Sn shot, Bi pieces, and Te shot in the ratio of  $1(\text{SnBi}_2\text{Te}_4):4\text{Te}$  were placed in a 2-ml alumina growth crucible of a Canfield crucible set [42]. The crucible set was then sealed under vacuum inside of a silica ampoule. The sealed ampoule was heated to  $900^\circ\text{C}$  to obtain a homogeneous melt and then cooled over 10 days to  $480^\circ\text{C}$ . At this temperature, Te flux was decanted from the  $\text{SnBi}_2\text{Te}_4$  single crystals. Single crystals of  $\text{Sn}_{1-x}\text{In}_x\text{Bi}_2\text{Te}_4$  were grown by heating a stoichiometric mixture of the starting elements at  $565^\circ\text{C}$  for over 2 weeks. The melting behavior of  $\text{Sn}_{1-x}\text{In}_x\text{Bi}_2\text{Te}_4$  was not found in the literature. Our test growths suggest that (1) In-rich  $\text{Sn}_{1-x}\text{In}_x\text{Bi}_2\text{Te}_4$  melts, most likely peritectically, around  $570^\circ\text{C}$ , and (2) the appropriate temperature window suitable for crystal growth is narrow, similar to  $\text{MnBi}_2\text{Te}_4$  [43]. The In content  $x$  in the  $\text{Sn}_{1-x}\text{In}_x\text{Bi}_2\text{Te}_4$  crystals grown for this study was limited to about 0.61. Attempts to increase this led to the formation of secondary phases coexisting with  $\text{Sn}_{\sim 0.4}\text{In}_{\sim 0.6}\text{Bi}_2\text{Te}_4$ . This suggests that the solubility limit of In in  $\text{SnBi}_2\text{Te}_4$  is near this value under the range of conditions used here. Increasing this value, or realizing  $\text{GeAs}_2\text{Te}_4$ -type  $\text{InBi}_2\text{Te}_4$ , may require different approaches (high pressure or significantly altered melt compositions for example).

The compositions of the crystals were measured using energy dispersive spectroscopy (EDS) with a Hitachi TM3000 scanning electron microscope and Bruker Quantax70 spectrometer. Data from at least three spots on at least three different crystals were used to calculate the average compositions. Powder x-ray diffraction using a PANalytical X'Pert Pro MPD diffractometer was used to confirm the single phase nature of the crystals and determine their lattice parameters at room temperature (measured patterns are shown in the Supplemental Material [44]). The diffraction samples were prepared by grinding single crystals.

Measurements of thermodynamic and electronic properties were performed using commercial cryostats from Quantum Design (Dynacool, PPMS, MPMS-3) with the addition of an adiabatic demagnetization refrigerator option for transport measurements,  $^3\text{He}$  options for transport, heat capacity, and ac and dc magnetization measurements, and a dilution refrigerator option for heat capacity measurements. Contacts for transport measurements were made using silver paste (Dupont 4929N). Thermal expansion (see Supplemental Material [44]) was measured in a CMR adiabatic demagnetization refrigerator with a capacitive dilatometer described in Ref. [45].

TABLE I.  $\text{Sn}_{1-x}\text{In}_x\text{Bi}_2\text{Te}_4$  crystal compositions, room temperature lattice parameters ( $a$ ,  $c$ ), normal state Sommerfeld coefficients ( $\gamma$ ), superconducting transition temperatures ( $T_c$ ), specific heat discontinuities at  $T_c$  ( $\Delta c_p$ ), and upper critical field at  $T = 0$  estimated in the WHH approximation for fields along the  $c$  axis ( $H_{c2}(0)^{\text{WHH}}$ ). For  $T_c$  in samples with  $x \geq 0.33$  the average and the standard deviation calculated from the three values determined from resistivity, magnetic susceptibility, and heat capacity data are listed.

EDS composition Sn:In:Bi:Te	$x$ in $\text{Sn}_{1-x}\text{In}_x\text{Bi}_2\text{Te}_4$	$a$ (Å)	$c$ (Å)	$\gamma$ (J mol-FU $^{-1}$ K $^{-2}$ )	$T_c$ (K)	$\Delta c_p(\gamma T_c)^{-1}$	$H_{c2}(0)^{\text{WHH}}$ (kOe)
0.99(1):0:1.96(2):4.05(2)	0	4.3942(2)	41.604(1)	0.0027(1)			
0.83(3):0.15(2):1.99(3):4.03(3)	0.16	4.3934(4)	41.452(3)		0.43		
0.68(1):0.34(1):1.97(2):4.02(2)	0.33	4.3900(4)	41.356(2)	0.0055(2)	1.22(5)	1.23	10.3
0.47(3):0.47(2):2.00(1):4.06(3)	0.50	4.3896(3)	41.242(2)	0.0065(1)	1.65(4)	1.45	13.2
0.38(1):0.59(2):2.00(1):4.03(2)	0.61	4.3870(4)	41.195(3)	0.0065(4)	1.85(5)	1.51	13.8

ARPES measurements were performed in a laboratory-based system using a Scienta DA30L electron spectrometer and an Oxide  $h\nu = 11$  eV laser light source. Bulk crystals were mounted to a sample holder using silver epoxy with a cleaving post mounted on top. The crystals were cleaved and measured at a base temperature of  $T \sim 8$  K and base pressure below  $5 \times 10^{-11}$  Torr by knocking off the top post. Linear polarization (p-wave) light was used, and the instrument was set for a total energy resolution of  $\sim 4$  meV and angular resolution of  $\sim 0.01^\circ$ .

Neutron diffraction data from a rectangular platelet-like crystal of  $\text{SnBi}_2\text{Te}_4$  with the dimensions of  $3.90 \times 2.98 \times 0.24$  mm $^3$  were measured on the TOPAZ single-crystal neutron diffractometer at the ORNL Spallation Neutron Source (SNS) [46]. The crystal was glued on the tip of a MiTe-Gen loop using Super Glue and transferred to the TOPAZ ambient goniometer for data collection at room temperature. The TOPAZ instrument uses the neutron wavelength-resolved Laue method for data collection by expanding the measured diffraction pattern from 2D on detector spaces ( $x$ ,  $y$ ) to wavelength-resolved 3D volume in ( $x$ ,  $y$ ,  $\lambda$ ) along the neutron time-of-flight direction. The sample orientations were optimized with the CrystalPlan software for better than 98% coverage based on crystal symmetry [47]. A total of nine sample orientations were used in data collection. Each of the sample orientations was measured for approximately 1 h with 5 C of proton charge with SNS beam power at 1.4 MW. The integrated raw Bragg intensities were obtained using the 3D ellipsoidal Q-space integration following previously reported methods [48]. Data reduction, including neutron TOF spectrum, Lorentz, and detector efficiency corrections, was carried out with the mantid python program [49]. The reduced data were saved in SHELX HKLF2 wavelength-resolved Laue format, in which the wavelength is recorded separately for each reflection, and data were not merged. Starting with the reported structure refined from our powder x-ray diffraction data, the crystal structure was refined using the JANA2020 program [50]. Refinement results are reported in the Supplemental Material [44].

### III. STRUCTURE AND COMPOSITION

The crystals' compositions determined by energy dispersive spectroscopy (EDS) are reported in Table I. The EDS results are normalized to give a total of seven atoms in the formula unit, and are consistent with the formula  $\text{ABi}_2\text{Te}_4$

with  $A = \text{Sn, In}$ . In the following, the samples will be referred to by the value of  $x$  in the chemical formula  $\text{Sn}_{1-x}\text{In}_x\text{Bi}_2\text{Te}_4$  determined by EDS (Table I).

All of the powder x-ray diffraction data from ground crystals of  $\text{Sn}_{1-x}\text{In}_x\text{Bi}_2\text{Te}_4$  were consistent with the  $\text{GeAs}_2\text{Te}_4$  structure type (see powder x-ray diffraction data in Supplemental Material [44]). The van der Waals layered structure is shown in Figs. 1(a) and 1(b), and the plate-like crystals are shown in Fig. 1(c). The lattice parameters refined from the powder x-ray diffraction data are plotted in Fig. 1(d), and substitution of In into  $\text{SnBi}_2\text{Te}_4$  is seen to compress the lattice both in the plane and along the stacking direction. Based on the measured stoichiometries (Table I), it is clear that In primarily replaces Sn as expected, and the decrease in lattice parameters with increasing In concentration is consistent with the reported behavior in  $\text{Sn}_{1-x}\text{In}_x\text{Te}$  [41,51].

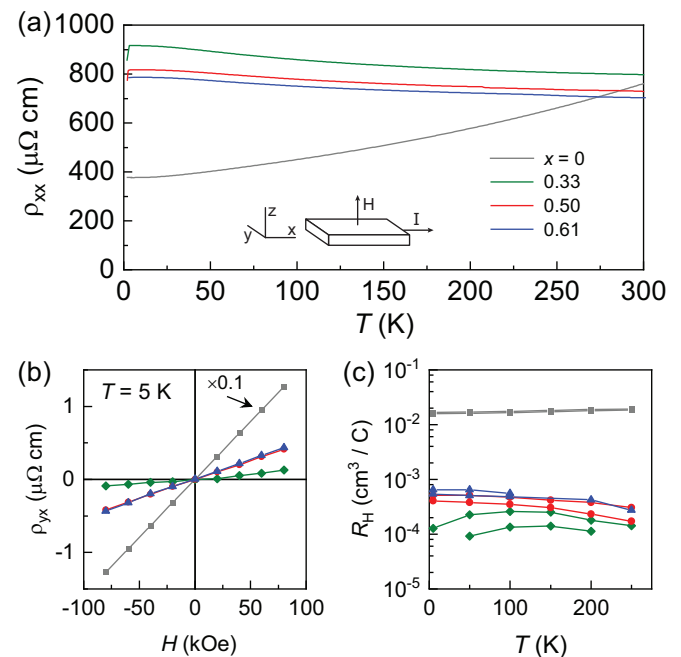


FIG. 2. Normal state electrical transport in  $\text{Sn}_{1-x}\text{In}_x\text{Bi}_2\text{Te}_4$ . (a) Resistivity measured in zero magnetic field. (b) Transverse resistivity measured in fields from  $-80$  to  $80$  kOe. The data has been antisymmetrized to exclude contributions from longitudinal voltages. (c) Hall coefficient determined from the slope of  $\rho_{yx}(H)$ . Panel (c) shows data from two samples of each composition.

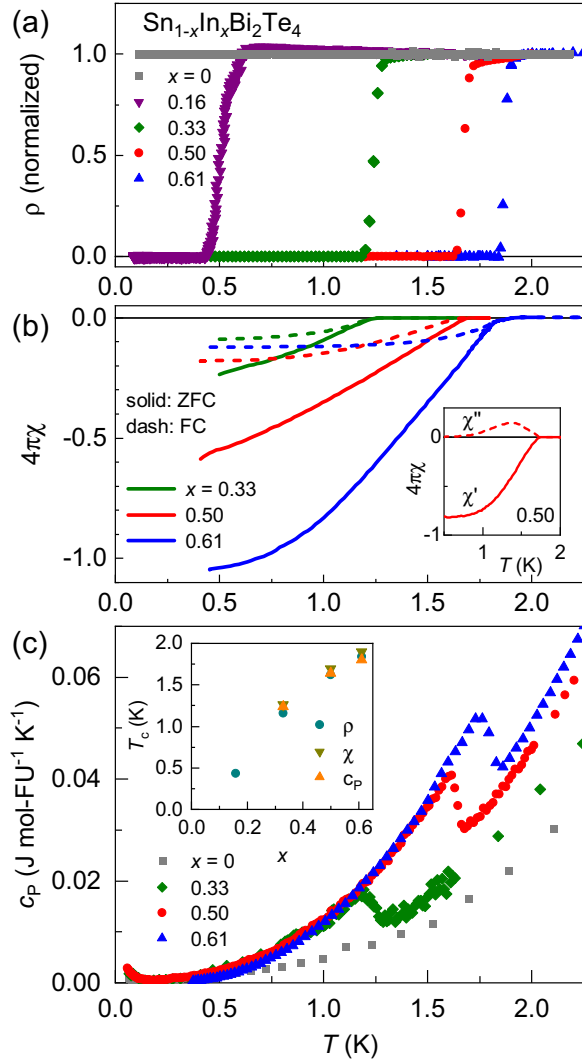


FIG. 3. Evidence for bulk superconductivity in  $\text{Sn}_{1-x}\text{In}_x\text{Bi}_2\text{Te}_4$ . (a) Resistivity, normalized in the normal state for comparison. (b) dc magnetic susceptibility, measured on warming in a 5 Oe in-plane field after zero-field cooling (ZFC) and field cooling (FC), with ac susceptibility results shown in the inset. (c) Specific heat capacity per formula unit (FU). The inset in (c) shows the values of  $T_c$  determined by the temperature at which  $\rho$  reaches zero, the onset of diamagnetism, and the midpoint of the heat capacity jump.

The structure of  $\text{SnBi}_2\text{Te}_4$  was further investigated using single crystal neutron diffraction at room temperature. Tables of results from the refinement of the neutron diffraction data can be found in the Supplemental Material [44]. This data is particularly useful for examining the degree of cation mixing, known to be common in this family of materials [52–54]. The refined Sn and Bi concentrations on their two crystallographic sites are shown in Fig. 1(a). Subtleties of how In may be distributed along with Sn and Bi on the two cation sites are beyond the scope of this paper, and the simple formula  $\text{Sn}_{1-x}\text{In}_x\text{Bi}_2\text{Te}_4$  suffices to describe the materials for the present purposes.

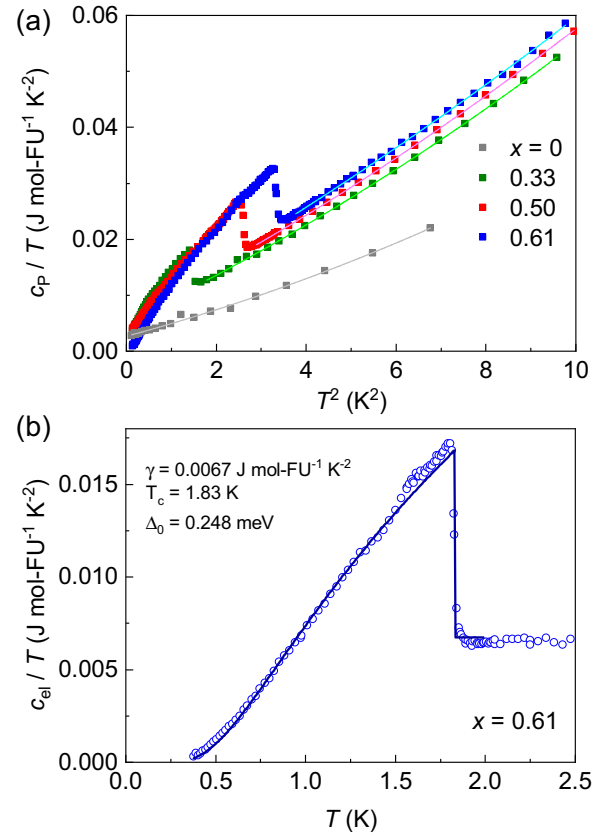


FIG. 4. (a) Fits to the normal state heat capacity data with fitted parameters reported in Table I and the Supplemental Material [44]. (b) A fit of the electronic heat capacity near and below  $T_c$  for  $\text{Sn}_{1-x}\text{In}_x\text{Bi}_2\text{Te}_4$  with  $x = 0.61$ . See text for details.

#### IV. PHYSICAL PROPERTIES

Results of resistivity and Hall effect measurements in the normal state are shown in Fig. 2.  $\text{SnBi}_2\text{Te}_4$  behaves like a poor metal, heavily doped semiconductor, or semimetal, with a resistivity changing by about a factor of two between room temperature and 2 K. Indium substitution has only a small effect on the value of the resistivity at room temperature, but changes the temperature dependence to show slight increases upon cooling. Similar behavior was observed when In was substituted into  $\text{SnTe}$  [40], although in that case the temperature dependence remained metal-like and the change in resistivity could be attributed to defect scattering increasing the residual resistivity.

In  $\text{Sn}_{1-x}\text{In}_x\text{Bi}_2\text{Te}_4$  transverse resistivities  $\rho_{yx}$  changed linearly with applied field at all temperatures, and are shown in Fig. 2(b) for  $T = 5$  K. The Hall coefficients determined from the slopes of  $\rho_{yx}$  vs  $H$  are shown in Fig. 2(c). Positive values indicate conduction is dominated by holes in all samples. Comparing  $\text{SnBi}_2\text{Te}_4$  to the indium containing samples shows that the substitution significantly reduces  $R_H$ . In a single band model this would indicate In dopes holes into the system, consistent with the relative positions of Sn and In on the periodic table. However, no clear trend is seen in  $R_H$  among the In containing samples. If two carrier types are present or multiple carrier pockets (Ref. [32]) become involved in

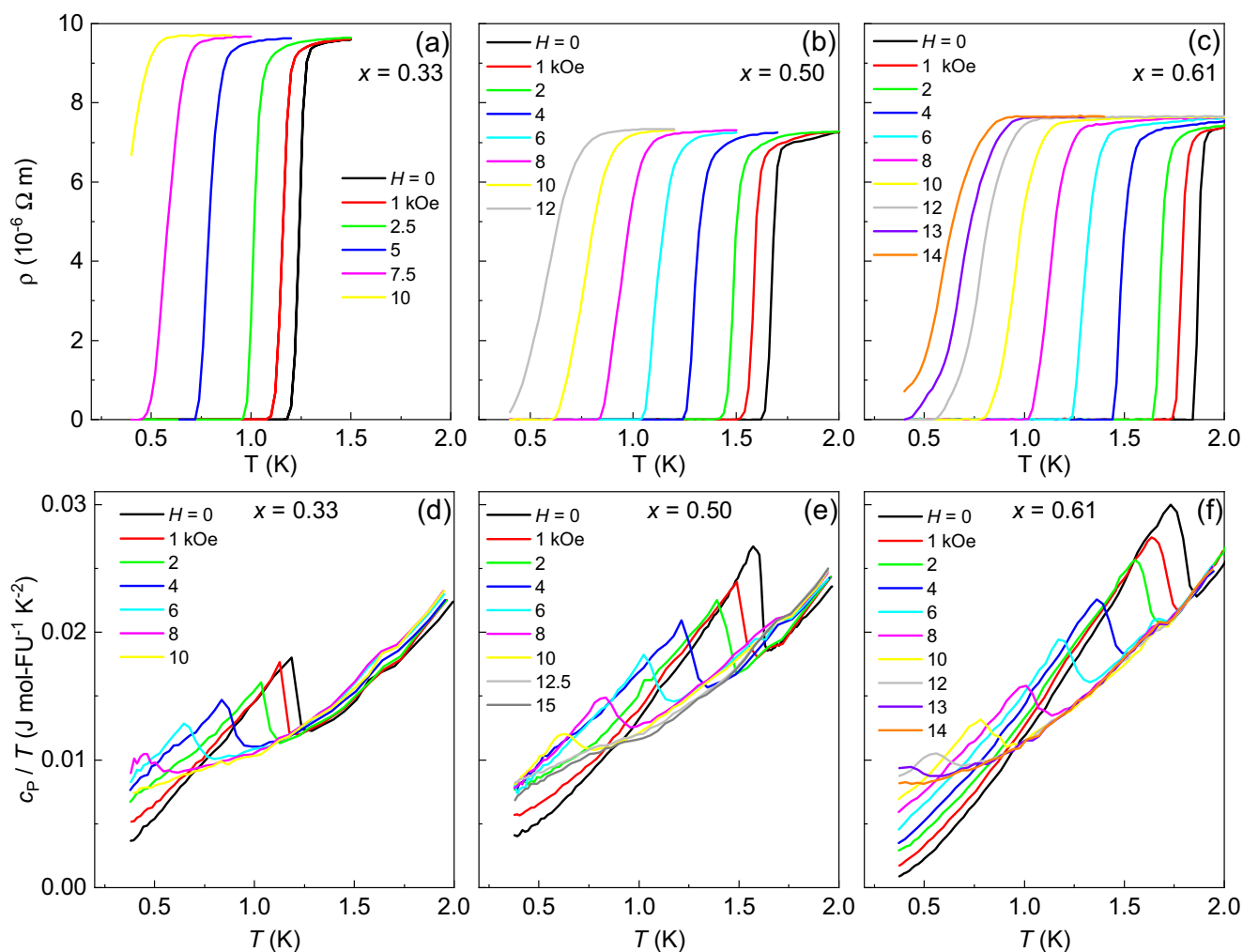


FIG. 5. Magnetic field dependence of superconducting transitions in  $\text{Sn}_{1-x}\text{In}_x\text{Bi}_2\text{Te}_4$  seen in electrical resistivity [(a)–(c)] and specific heat capacity plotted as  $c_p/T$  [(d)–(f)].

the transport, the interpretation of the change in  $R_H$  with  $x$  is not straightforward. Nevertheless, the data does suggest that indium introduces holes into the system, although the electronic response to such high levels of substitution goes beyond any simple doping picture as clearly demonstrated for indium substitution in  $\text{SnTe}$  [51]. Increasing hole conduction upon indium substitution is supported by Seebeck coefficient measurements on crystals with  $x = 0$  and  $x = 0.61$  as well (see Supplemental Material [44] and [36]). The Seebeck coefficient for  $\text{SnBi}_2\text{Te}_4$  measured at 300 K is  $76 \mu\text{V}/\text{K}$ , indicating  $p$ -type behavior and in agreement with previous reports [36]. Indium substitution decreases this value to  $23 \mu\text{V}/\text{K}$  for  $x = 0.61$ .

The superconducting transitions in  $\text{Sn}_{1-x}\text{In}_x\text{Bi}_2\text{Te}_4$  are demonstrated in Fig. 3. This figure shows results of electrical resistance, magnetization, and heat capacity measurements. Figure 3(a) shows sharp transitions to zero resistance states for  $x \geq 0.16$ , and we define  $T_c$  as the temperature at which the resistance reaches zero. The dc magnetic susceptibility data shown in the main panel of Fig. 3(b) demonstrate large superconducting volume fractions, and show divergence between zero-field-cooled and field-cooled data. The latter is an indication of type-II superconductivity and the

presence of a mixed state when cooling through  $T_c$  in an applied field. We define the transition temperature from this data as the onset of diamagnetism. The inset shows results of ac magnetic susceptibility for a crystal with  $x = 0.50$ . The specific heat capacity data in Fig. 3(c) reveals sharp  $\lambda$  anomalies at the superconducting phase transition, and we define  $T_c$  as the midpoint of the specific heat capacity jump.

The inset in Fig. 3(c) shows the  $T_c$  values determined as described above. Good agreement is seen among the values determined from three types of measurements. The transition temperature increases with  $x$  up to the maximum indium content achieved in this study ( $x = 0.61$ ). Table I contains the  $T_c$  values. For  $x \geq 0.33$  the average and the standard deviation calculated from the three values determined from resistivity, magnetic susceptibility, and heat capacity data are listed. It is likely that the dependence of  $T_c$  on  $x$  in  $\text{Sn}_{1-x}\text{In}_x\text{Bi}_2\text{Te}_4$  is primarily related to changes in the chemical potential associated with In substitution. As noted above, the introduction of In does compress the lattice [Fig. 1(d)], but the roles played by electronic tuning and chemical pressure in determining the ground state cannot be distinguished reliably using the present data.

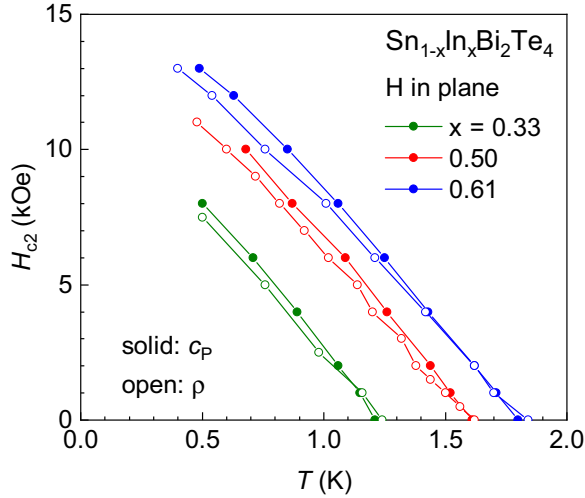


FIG. 6. Superconducting phase diagrams for  $\text{Sn}_{1-x}\text{In}_x\text{Bi}_2\text{Te}_4$  determined from  $c_p$  and  $\rho$  measurements performed in magnetic fields directed out of the plane (parallel to the  $c$  axis). Data used to construct the plots are shown in Fig. 5.

The low-temperature specific heat capacity data was analyzed as shown in Fig. 4(a). Data in the normal state is well described by  $c_p(T) = \gamma T + \beta T^3 + \delta T^5$ , where the first term is the electronic contribution (with Sommerfeld coefficient,  $\gamma$ ) and the second and third terms describe the phonon contribution. The data are plotted as  $c_p/T$  vs  $T^2$ , and the slight curvature seen in the plots warranted inclusion of the  $\delta T^5$  term. The  $\gamma$  values determined from the fits are listed in Table I, and other fitted parameters are reported in the Supplemental Material [44]. Fitted  $\gamma$  values show a general increase with increasing  $x$ . This is consistent with indium substitution increasing the carrier concentration in  $\text{Sn}_{1-x}\text{In}_x\text{Bi}_2\text{Te}_4$ . Weak coupling BCS theory predicts a specific heat discontinuity ( $\Delta c_p$ ) at  $T_c$  of  $1.43\gamma T_c$ . The measured ratios  $\Delta c_p/(\gamma T_c)$  are shown in Table I, and are close to the BCS weak coupling value.

Specific heat capacity data for the highest  $T_c$  material ( $x = 0.61$ ) was modeled assuming BCS behavior [55],

$$C_{\text{BCS}} = t \frac{d}{dt} \int_0^\infty dy \left( -\frac{6\gamma\Delta_0}{k_B\pi^2} \right) [f \ln f + (1-f) \ln(1-f)],$$

where  $t = T/T_c$ ,  $f = 1/[\exp(E/k_B T) + 1]$ ,  $E = (\epsilon^2 + \Delta^2)^{1/2}$ ,  $y = \epsilon/\Delta_0$ , and  $\Delta(T)/\Delta_0$  is the BCS temperature dependence of the gap taken from the tables of Mühlischlegel [56].

The data are well fit using a single superconducting gap  $\Delta_0$  along with  $\gamma$  and  $T_c$  as three free parameters, and the fitted curve and parameters are shown in Fig. 4(b). The fitted  $T_c$  and  $\gamma$  are consistent with the other determinations presented here (Table I). The fitted gap is 0.248 meV, or  $1.80 k_B T_c$ . This is very close to the BCS weak-coupling value of  $\Delta/(k_B T_c) = 1.76$ . Double integration of the fitted specific heat curve from 0 to  $T_c$  gives the condensation energy of 4.8 mJ/mol-FU. The condensation energy is equal to  $H_c^2/8\pi$  from which we obtain a thermodynamic critical field of 94 Oe.

To understand the superconducting phase diagram of  $\text{Sn}_{1-x}\text{In}_x\text{Bi}_2\text{Te}_4$ , the effects of magnetic fields applied

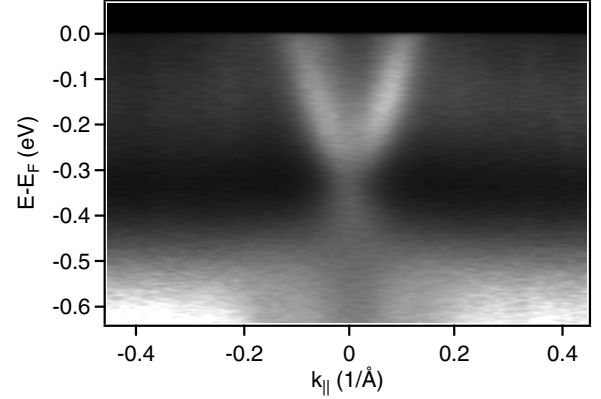


FIG. 7. ARPES data for  $\text{Sn}_{1-x}\text{In}_x\text{Bi}_2\text{Te}_4$  with  $x = 0.5$  at the Brillouin zone center showing the linear dispersion from the topological Dirac surface states. Data were measured at a  $T \sim 8$  K.

parallel to the  $c$  axis were investigated using electrical resistivity and heat capacity measurements for  $x = 0.33, 0.50, 0.61$ . The data are shown in Fig. 5. The magnetic field suppresses superconductivity as expected. A plot of applied field vs  $T_c$  determined from these measurements traces the upper critical field  $H_{c2}$ . These curves are shown in Fig. 6. The Werthamer-Helfand-Hohenberg (WHH) theory gives an estimate of critical field at zero temperature based on the slope near  $T_c$  in low fields:  $H_{c2}(0) = -0.69T_c(dH_{c2}/dT)|_{T=T_c}$ . Table I contains the results obtained by applying this to the phase diagram data derived from specific heat measurements. The  $H_{c2}(0)$  values determined in this way are consistent with the behaviors seen down to the lowest temperatures studied (Fig. 6). For  $x = 0.61$  we find  $H_{c2}(0) = 13.8$  kOe. Comparing this with the thermodynamic critical field of 94 Oe obtained from our heat capacity fit firmly establishes this compound as a type II superconductor. The broadening of the superconducting transition in response to the applied field (see Fig. 5) supports this conclusion.

Returning to the topological nature of these materials, we recall that previous reports reveal Dirac surface states for  $\text{SnBi}_2\text{Te}_4$  establishing the material as a topological insulator [31]. While the calculated band structure for  $\text{SnBi}_2\text{Te}_4$  predicts a topological insulating band structure with the Dirac point located at  $E - E_F \sim 0.1$  eV, the measured bands structure showed the Dirac point to be located at the Fermi level [24,31]. To confirm that topological surface states also exist in the superconducting indium substituted materials, ARPES data were collected in the normal state of an  $\text{Sn}_{1-x}\text{In}_x\text{Bi}_2\text{Te}_4$  crystal with  $x = 0.5$  at the Brillouin zone center ( $\Gamma$ ) (see Methods). We indeed observe the linearly dispersing topological surface states with the Dirac point located at  $E - E_F = -0.35$  eV as shown in Fig. 7. The measured band structure suggests a shift of the electronic structure due to the alloying and shows the topological nature persists in superconducting  $\text{Sn}_{1-x}\text{In}_x\text{Bi}_2\text{Te}_4$  crystals.

## V. SUMMARY AND CONCLUSIONS

In summary, we have identified  $\text{Sn}_{1-x}\text{In}_x\text{Bi}_2\text{Te}_4$  as an interesting cleavable material for the study of the interplay of

nontrivial electronic topology and superconductivity.  $\text{SnBi}_2\text{Te}_4$  is known to be a topological insulator [24–26,31,32]. Here we show that indium substitution induces bulk superconductivity in  $\text{Sn}_{1-x}\text{In}_x\text{Bi}_2\text{Te}_4$  while maintaining the presence of topological surface states near the Fermi level. For the highest indium concentrations,  $T_c$  and  $H_{c2}(0)$  reach approximately 1.85 K and 14 kOe, respectively. The specific heat capacity follows BCS behavior. The superconductivity is type-II, which could support vortices hosting Majorana zero modes in the Fu-Kane model [5]. The next steps are to experimentally and theoretically understand in detail how the topological surface states evolve with In content, how they interact with the superconductivity, and its resulting topological nature. While this paper has been considered primarily within the context of the Fu-Kane model [5], the centrosymmetric structure and strong spin-orbit coupling make  $\text{Sn}_{1-x}\text{In}_x\text{Bi}_2\text{Te}_4$  potentially compatible with the Fu-Berg model for bulk topological superconductivity as well, as proposed for Cu-doped  $\text{Bi}_2\text{Se}_3$  [6]. Importantly,  $\text{SnBi}_2\text{Te}_4$  is a member of a large family of similar natural heterostructures, and as noted above, many are expected to have nontrivial topology. This suggests study of not only  $AM_2X_4$  (or  $AX \cdot M_2X_3$ ) with  $A = \text{Ge}, \text{Sn}, \text{Pb}$ ,  $M = \text{As}, \text{Sb}$ ,

$\text{Bi}$ , and  $X = \text{Se}, \text{Te}$ , but also  $n(\text{AX}) \cdot M_2X_3$  with thicker  $AX$  slabs,  $AX \cdot m(M_2X_3)$  with additional  $M_2X_3$  layers, and, in principle,  $n(\text{AX}) \cdot m(M_2X_3)$ . There are numerous opportunities to explore the effects of not only alloying as demonstrated here but also intercalation [57] in these materials. Clearly there is much interesting work to be done and we hope the present study motivates further research exploring  $\text{Sn}_{1-x}\text{In}_x\text{Bi}_2\text{Te}_4$  and related compounds as a new family of candidate topological superconductors.

## ACKNOWLEDGMENTS

This material is based upon work supported by the U.S. Department of Energy, Office of Science, National Quantum Information Science Research Centers, Quantum Science Center. AFM acknowledges support from the U.S. Department of Energy, Office of Science, Basic Energy Sciences, Materials Sciences and Engineering Division (heat capacity measurements). A portion of this research used resources at the Spallation Neutron Source, a DOE Office of Science User Facility operated by the Oak Ridge National Laboratory.

- 
- [1] C.-Z. Chang, J. Zhang, X. Feng, J. Shen, Z. Zhang, M. Guo, K. Li, Y. Ou, P. Wei, L.-L. Wang *et al.*, Experimental observation of the quantum anomalous Hall effect in a magnetic topological insulator, *Science* **340**, 167 (2013).
- [2] H. Weng, R. Yu, X. Hu, X. Dai, and Z. Fang, Quantum anomalous Hall effect and related topological electronic states, *Adv. Phys.* **64**, 227 (2015).
- [3] D. Xiao, J. Jiang, J.-H. Shin, W. Wang, F. Wang, Y.-F. Zhao, C. Liu, W. Wu, M. H. W. Chan, N. Samarth, and C.-Z. Chang, Realization of the Axion Insulator State in Quantum Anomalous Hall Sandwich Heterostructures, *Phys. Rev. Lett.* **120**, 056801 (2018).
- [4] D. F. Liu, A. J. Liang, E. K. Liu, Q. N. Xu, Y. W. Li, C. Chen, D. Pei, W. J. Shi, S. K. Mo, P. Dudin *et al.*, Magnetic Weyl semimetal phase in a Kagomé crystal, *Science* **365**, 1282 (2019).
- [5] L. Fu and C. L. Kane, Superconducting Proximity Effect and Majorana Fermions at the Surface of a Topological Insulator, *Phys. Rev. Lett.* **100**, 096407 (2008).
- [6] L. Fu and E. Berg, Odd-Parity Topological Superconductors: Theory and Application to  $\text{Cu}_x\text{Bi}_2\text{Se}_3$ , *Phys. Rev. Lett.* **105**, 097001 (2010).
- [7] M. Sato and Y. Ando, Topological superconductors: A review, *Rep. Prog. Phys.* **80**, 076501 (2017).
- [8] S. Frolov, M. Manfra, and J. Sau, Topological superconductivity in hybrid devices, *Nat. Phys.* **16**, 718 (2020).
- [9] R. M. Lutchyn, J. D. Sau, and S. Das Sarma, Majorana Fermions and a Topological Phase Transition in Semiconductor-Superconductor Heterostructures, *Phys. Rev. Lett.* **105**, 077001 (2010).
- [10] P. Zhang, K. Yaji, T. Hashimoto, Y. Ota, T. Kondo, K. Okazaki, Z. Wang, J. Wen, G. Gu, H. Ding, and S. Shin, Observation of topological superconductivity on the surface of an iron-based superconductor, *Science* **360**, 182 (2018).
- [11] J. Li, Y. Li, S. Du, Z. Wang, B.-L. Gu, S.-C. Zhang, K. He, W. Duan, and Y. Xu, Intrinsic magnetic topological insulators in van der Waals layered  $\text{MnBi}_2\text{Te}_4$ -family materials, *Sci. Adv.* **5**, eaaw5685 (2019).
- [12] K. He,  $\text{MnBi}_2\text{Te}_4$ -family intrinsic magnetic topological materials, *npj Quantum Mater.* **5**, 90 (2020).
- [13] Y. Deng, Y. Yu, M. Z. Shi, Z. Guo, Z. Xu, J. Wang, X. H. Chen, and Y. Zhang, Quantum anomalous Hall effect in intrinsic magnetic topological insulator  $\text{MnBi}_2\text{Te}_4$ , *Science* **367**, 895 (2020).
- [14] C. Liu, Y. Wang, H. Li, Y. Wu, Y. Li, J. Li, K. He, Y. Xu, J. Zhang, and Y. Wang, Robust axion insulator and Chern insulator phases in a two-dimensional antiferromagnetic topological insulator, *Nat. Mater.* **19**, 522 (2020).
- [15] J. Ge, Y. Liu, J. Li, H. Li, T. Luo, Y. Wu, Y. Xu, and J. Wang, High-Chern-number and high-temperature quantum Hall effect without Landau levels, *Nat. Sci. Rev.* **7**, 1280 (2020).
- [16] D. Ovchinnikov, X. Huang, Z. Lin, Z. Fei, J. Cai, T. Song, M. He, Q. Jiang, C. Wang, H. Li *et al.*, Intertwined topological and magnetic orders in atomically thin Chern insulator  $\text{MnBi}_2\text{Te}_4$ , *Nano Lett.* **21**, 2544 (2021).
- [17] Y.-F. Zhao, L.-J. Zhou, F. Wang, G. Wang, T. Song, D. Ovchinnikov, H. Yi, R. Mei, K. Wang, M. H. W. Chan *et al.*, Even-odd layer-dependent anomalous Hall effect in topological magnet  $\text{MnBi}_2\text{Te}_4$  thin films, *Nano Lett.* **21**, 7691 (2021).
- [18] D. A. Ivanov, Non-Abelian Statistics of Half-Quantum Vortices in p-Wave Superconductors, *Phys. Rev. Lett.* **86**, 268 (2001).
- [19] Z. Wang, P. Zhang, G. Xu, L. K. Zeng, H. Miao, X. Xu, T. Qian, H. Weng, P. Richard, A. V. Fedorov, H. Ding, X. Dai, and Z. Fang, Topological nature of the  $\text{FeSe}_{0.5}\text{Te}_{0.5}$  superconductor, *Phys. Rev. B* **92**, 115119 (2015).
- [20] L. Kuznetsova, V. Kuznetsov, and D. Rowe, Thermoelectric properties and crystal structure of ternary compounds in the  $\text{Ge}(\text{Sn},\text{Pb})\text{Te}-\text{Bi}_2\text{Te}_3$  systems, *J. Phys. Chem. Solids* **61**, 1269 (2000).

- [21] L. Shelimova, O. Karpinskii, P. Konstantinov, E. Avilov, M. Kretova, and V. Zemskov, Crystal structures and thermoelectric properties of layered compounds in the ATe-Bi<sub>2</sub>Te<sub>3</sub> (A = Ge, Sn, Pb) systems, *Inorg. Mater.* **40**, 451 (2004).
- [22] L. Zhang and D. J. Singh, Electronic structure and thermoelectric properties of PbBi<sub>2</sub>Te<sub>4</sub> and related intergrowth compounds, *Phys. Rev. B* **81**, 245119 (2010).
- [23] H. Jin, J.-H. Song, A. J. Freeman, and M. G. Kanatzidis, Candidates for topological insulators: Pb-based chalcogenide series, *Phys. Rev. B* **83**, 041202(R) (2011).
- [24] S. V. Eremeev, G. Landolt, T. V. Menshchikova, B. Slomski, Y. M. Koroteev, Z. S. Aliev, M. B. Babanly, J. Henk, A. Ernst, L. Patthey, A. Eich, H. J. P. O. Khajetoorians, A. A., J. Wiebe, R. Wiesendanger, P. M. Echeniquo, S. S. Tsirkin, I. R. Amiraslanov, J. H. Dil, and E. V. Chulkov, Atom-specific spin mapping and buried topological states in a homologous series of topological insulators, *Nat. Commun.* **3**, 635 (2012).
- [25] T. V. Menshchikova, S. V. Eremeev, Y. M. Koroteev, V. M. Kuznetsov, and E. V. Chulkov, Ternary compounds based on binary topological insulators as an efficient way for modifying the Dirac cone, *JETP Lett.* **93**, 15 (2011).
- [26] M. G. Vergniory, T. V. Menshchikova, I. V. Silkin, Yu. M. Koroteev, S. V. Eremeev, and E. V. Chulkov, Electronic and spin structure of a family of Sn-based ternary topological insulators, *Phys. Rev. B* **92**, 045134 (2015).
- [27] L.-L. Wang, Highly tunable band inversion in AB<sub>2</sub>X<sub>4</sub> (A = Ge, Sn, Pb; B = As, Sb, Bi; X = Se, Te) compounds, *Phys. Rev. Mater.* **6**, 094201 (2022).
- [28] M. Nurmatamat, K. Okamoto, S. Zhu, T. V. Menshchikova, I. P. Rusinov, V. O. Korostelev, K. Miyamoto, T. Okuda, T. Miyashita, X. Wang *et al.*, Topologically nontrivial phase-change compound GeSb<sub>2</sub>Te<sub>4</sub>, *ACS Nano* **14**, 9059 (2020).
- [29] M. Neupane, S.-Y. Xu, L. A. Wray, A. Petersen, R. Shankar, N. Alidoust, C. Liu, A. Fedorov, H. Ji, J. M. Allred, Y. S. Hor, T.-R. Chang, H.-T. Jeng, H. Lin, A. Bansil, R. J. Cava, and M. Z. Hasan, Topological surface states and Dirac point tuning in ternary topological insulators, *Phys. Rev. B* **85**, 235406 (2012).
- [30] K. Okamoto, K. Kuroda, H. Miyahara, K. Miyamoto, T. Okuda, Z. S. Aliev, M. B. Babanly, I. R. Amiraslanov, K. Shimada, H. Namatame, M. Taniguchi, D. A. Samorokov, T. V. Menshchikova, E. V. Chulkov, and A. Kimura, Observation of a highly spin-polarized topological surface state in GeBi<sub>2</sub>Te<sub>4</sub>, *Phys. Rev. B* **86**, 195304 (2012).
- [31] Y. Li, C. Huang, G. Wang, J. Hu, S. Duan, C. Xu, Q. Lu, Q. Jing, W. Zhang, and D. Qian, Topological Dirac surface states in ternary compounds GeBi<sub>2</sub>Te<sub>4</sub>, SnBi<sub>2</sub>Te<sub>4</sub> and Sn<sub>0.571</sub>Bi<sub>2.286</sub>Se<sub>4</sub>, *Chin. Phys. B* **30**, 127901 (2021).
- [32] S. Fragkos, L. Baringthon, P. Tsipas, E. Xenogiannopoulou, P. Le Fèvre, P. Kumar, H. Okuno, N. Reyren, A. Lemaitre, G. Patriarche, J.-M. George, and A. Dimoulas, Topological surface states in epitaxial (SnBi<sub>2</sub>Te<sub>4</sub>)<sub>n</sub>(Bi<sub>2</sub>Te<sub>3</sub>)<sub>m</sub> natural van der Waals superlattices, *Phys. Rev. Mater.* **5**, 014203 (2021).
- [33] D. Niesner, S. Otto, V. Hermann, T. Fauster, T. V. Menshchikova, S. V. Eremeev, Z. S. Aliev, I. R. Amiraslanov, M. B. Babanly, P. M. Echenique, and E. V. Chulkov, Bulk and surface electron dynamics in a p-type topological insulator SnSb<sub>2</sub>Te<sub>4</sub>, *Phys. Rev. B* **89**, 081404(R) (2014).
- [34] K. Kuroda, H. Miyahara, M. Ye, S. V. Eremeev, Y. M. Koroteev, E. E. Krasovskii, E. V. Chulkov, S. Hiramoto, C. Moriyoshi, Y. Kuroiwa, K. Miyamoto, T. Okuda, M. Arita, K. Shimada, H. Namatame, M. Taniguchi, Y. Ueda, and A. Kimura, Experimental Verification of PbBi<sub>2</sub>Te<sub>4</sub> as a 3D Topological Insulator, *Phys. Rev. Lett.* **108**, 206803 (2012).
- [35] T. B. Zhukova and A. I. Zaslavsky, Crystal structures of the compounds PbBi<sub>4</sub>Te, PbBi<sub>2</sub>Te<sub>4</sub>, SnBi<sub>2</sub>Te<sub>7</sub>, SnSb<sub>2</sub>Te<sub>4</sub>, and GeBi<sub>4</sub>Te<sub>7</sub>, *Sov. Phys. Crystallogr.* **16**, 796 (1972).
- [36] B. A. Kuropatwa and H. Kleinke, Thermoelectric properties of stoichiometric compounds in the (SnTe)<sub>x</sub>(Bi<sub>2</sub>Te<sub>3</sub>)<sub>y</sub> system, *Z. Anorg. Allg. Chem.* **638**, 2640 (2012).
- [37] Y. Matsushita, P. A. Wiannecki, A. T. Sommer, T. H. Geballe, and I. R. Fisher, Type II superconducting parameters of TI-doped PbTe determined from heat capacity and electronic transport measurements, *Phys. Rev. B* **74**, 134512 (2006).
- [38] M. Katsuno, R. Jha, K. Hoshi, R. Sogabe, Y. Goto, and Y. Mizuguchi, High-pressure synthesis and superconducting properties of NaCl-type In<sub>1-x</sub>Pb<sub>x</sub>Te (x = 0-0.8), *Condensed Matter* **5**, 14 (2020).
- [39] M. P. Smylie, K. Kobayashi, J. Z. Dans, H. Hebbeker, R. Chapai, W.-K. Kwok, and U. Welp, Full superconducting gap in the candidate topological superconductor In<sub>1-x</sub>Pb<sub>x</sub>Te for x = 0.2, *Phys. Rev. B* **106**, 054503 (2022).
- [40] G. Balakrishnan, L. Bawden, S. Cavendish, and M. R. Lees, Superconducting properties of the In-substituted topological crystalline insulator SnTe, *Phys. Rev. B* **87**, 140507(R) (2013).
- [41] R. D. Zhong, J. A. Schneeloch, X. Y. Shi, Z. J. Xu, C. Zhang, J. M. Tranquada, Q. Li, and G. D. Gu, Optimizing the superconducting transition temperature and upper critical field of Sn<sub>1-x</sub>In<sub>x</sub>Te, *Phys. Rev. B* **88**, 020505(R) (2013).
- [42] P. C. Canfield, T. Kong, U. S. Kaluarachchi, and N. H. Jo, Use of frit-disc crucibles for routine and exploratory solution growth of single crystalline samples, *Philos. Mag.* **96**, 84 (2016).
- [43] J.-Q. Yan, Q. Zhang, T. Heitmann, Z. Huang, K. Y. Chen, J.-G. Cheng, W. Wu, D. Vaknin, B. C. Sales, and R. J. McQueeney, Crystal growth and magnetic structure of MnBi<sub>2</sub>Te<sub>4</sub>, *Phys. Rev. Mater.* **3**, 064202 (2019).
- [44] See Supplemental Material at <http://link.aps.org/supplemental/10.1103/PhysRevMaterials.7.034802> for powder x-ray diffraction patterns, single crystal neutron diffraction refinement results, normal-state heat capacity fitting results, Seebeck coefficient data, and thermal expansion data.
- [45] G. Schmiedeshoff, A. Lounsbury, D. Luna, S. Tracy, A. Schramm, S. Tozer, V. Correa, S. Hannahs, T. Murphy, E. Palm *et al.*, Versatile and compact capacitive dilatometer, *Rev. Sci. Instrum.* **77**, 123907 (2006).
- [46] L. Coates, H. Cao, B. C. Chakoumakos, M. D. Frontzek, C. Hoffmann, A. Y. Kovalevsky, Y. Liu, F. Meilleur, A. M. dos Santos, D. A. A. Myles *et al.*, A suite-level review of the neutron single-crystal diffraction instruments at Oak Ridge National Laboratory, *Rev. Sci. Instrum.* **89**, 092802 (2018).
- [47] J. Zikovsky, P. F. Peterson, X. P. Wang, M. Frost, and C. Hoffmann, CrystalPlan: An experiment-planning tool for crystallography, *J. Appl. Cryst.* **44**, 418 (2011).
- [48] A. J. Schultz, M. R. V. Jørgensen, X. Wang, R. L. Mikkelsen, D. J. Mikkelsen, V. E. Lynch, P. F. Peterson, M. L. Green, and C. M. Hoffmann, Integration of neutron time-of-flight single-crystal Bragg peaks in reciprocal space, *J. Appl. Cryst.* **47**, 915 (2014).
- [49] T. M. Michels-Clark, A. T. Savici, V. E. Lynch, X. Wang, and C. M. Hoffmann, Expanding Lorentz and spectrum corrections to large volumes of reciprocal space for single-crystal



- time-of-flight neutron diffraction, *J. Appl. Cryst.* **49**, 497 (2016).
- [50] V. Petříček, M. Dušek, and L. Palatinus, Crystallographic computing system JANA2006: General features, *Z. Kristallogr. Cryst. Mater.* **229**, 345 (2014).
- [51] N. Haldolaarachchige, Q. Gibson, W. Xie, M. B. Nielsen, S. Kushwaha, and R. J. Cava, Anomalous composition dependence of the superconductivity in In-doped SnTe, *Phys. Rev. B* **93**, 024520 (2016).
- [52] Y.-C. Zou, Z.-G. Chen, E. Zhang, F. Kong, Y. Lu, L. Wang, J. Drennan, Z. Wang, F. Xiu, K. Cho, and J. Zou, Atomic disorders in layer structured topological insulator SnBi<sub>2</sub>Te<sub>4</sub> nanoplates, *Nano Res.* **11**, 696 (2018).
- [53] Y. Liu, L.-L. Wang, Q. Zheng, Z. Huang, X. Wang, M. Chi, Y. Wu, B. C. Chakoumakos, M. A. McGuire, B. C. Sales, W. Wu, and J. Yan, Site Mixing for Engineering Magnetic Topological Insulators, *Phys. Rev. X* **11**, 021033 (2021).
- [54] H. Zhang, L. Lu, and S. Mi, Cation disorder and thermoelectric properties in layered ternary compounds MBi<sub>2</sub>Te<sub>4</sub> (M = Ge, Sn), *J. Mater. Chem. C* **10**, 854 (2022).
- [55] H. Padamsee, J. Neighbor, and C. Shiffman, Quasiparticle phenomenology for thermodynamics of strong-coupling superconductors, *J. Low Temp. Phys.* **12**, 387 (1973).
- [56] B. Mühlshlegel, Die thermodynamischen funktionen des supraleiters, *Z. Phys.* **155**, 313 (1959).
- [57] S. Sasaki, K. Segawa, and Y. Ando, Superconductor derived from a topological insulator heterostructure, *Phys. Rev. B* **90**, 220504(R) (2014).